PAPER • OPEN ACCESS

Connecting macroscopic dynamics with microscopic properties in active microtubule network contraction

View the article online for updates and enhancements.

New Journal of Physics

The open access journal at the forefront of physics

PAPER

CrossMark

Connecting macroscopic dynamics with microscopic properties in active microtubule network contraction

Peter J Foster[1,5] ⓘ, Wen Yan[2,5] ⓘ, Sebastian Fürthauer[2], Michael J Shelley[2,3] and Daniel J Needleman[1,4]

1 John A. Paulson School of Engineering and Applied Sciences, FAS Center for Systems Biology, Harvard University, Cambridge, MA, United States of America
2 Center for Computational Biology, Flatiron Institute, Simons Foundation, New York, NY, United States of America
3 Courant Institute of Mathematical Science, New York University, New York, NY, United States of America
4 Department of Molecular and Cellular Biology, Harvard University, Cambridge, MA, United States of America
5 Equal contribution.

E-mail: peterfoster@fas.harvard.edu and wyan@flatironinstitute.org

Keywords: active matter, microtubule, motor protein, dynein, Xenopus extract

Supplementary material for this article is available online

Abstract

The cellular cytoskeleton is an active material, driven out of equilibrium by molecular motor proteins. It is not understood how the collective behaviors of cytoskeletal networks emerge from the properties of the network's constituent motor proteins and filaments. Here we present experimental results on networks of stabilized microtubules in *Xenopus* oocyte extracts, which undergo spontaneous bulk contraction driven by the motor protein dynein, and investigate the effects of varying the initial microtubule density and length distribution. We find that networks contract to a similar final density, irrespective of the length of microtubules or their initial density, but that the contraction timescale varies with the average microtubule length. To gain insight into why this microscopic property influences the macroscopic network contraction time, we developed simulations where microtubules and motors are explicitly represented. The simulations qualitatively recapitulate the variation of contraction timescale with microtubule length, and allowed stress contributions from different sources to be estimated and decoupled.

1. Introduction

Active matter is a class of materials held out of equilibrium by the local conversion of energy from a reservoir into mechanical work at the scale of the system's components [1]. Active matter can exhibit emergent behaviors, such as collective motion and pattern formation, on lengthscales much larger than the size of the system's constituents.

Here we consider cytoskeletal networks, which are living, active systems [2] composed of polar polymeric filaments and held out of equilibrium by molecular motor proteins which convert chemical energy into mechanical work. Cytoskeletal networks are responsible for a number of cell biological processes, including cell division and chromosome segregation. The active behaviors of cytoskeletal networks have been experimentally investigated in both simplified purified mixtures [3–6] and in complex systems in cells and cell extracts [7–10]. However, it remains poorly understood how the dynamics and architecture of these networks are shaped by the properties of their constituent filaments and motors.

The past several years have seen several studies of the dynamics and mechanics of microtubule (MTs) / motor protein suspensions (see [11] for a review). A predominant thread of experiments have focused on dense, nematically aligned phases of MT bundles and immersed layers which show dynamics driven by extension of material along the direction of orientational order [12]. It is believed that this extensile motion is driven by the polarity sorting of anti-aligned MTs by multimeric kinesin motors. Theoretical modeling of the material stresses produced by polarity sorting indeed yields active stress tensors that are anisotropic, and arise from ensemble

averages of terms of the form $\alpha \boldsymbol{pp}$, where $\boldsymbol{p}$ is an MT orientation vector, and $\alpha < 0$ gives extensile flows along the $\boldsymbol{p}$ direction [13]. Different dynamics can follow from different MT interactions, and clustering of MT ends is a generic mechanism leading to contraction [14]. This has been previously explored in other purified systems containing kinesin motor proteins [15, 16]. In this work, as in our earlier work of stabilized MTs in meiotically-arrested *Xenopus* oocyte extracts [7] and in several related studies [17–19], we consider a spontaneously formed MT network whose dynamics is driven by minus-end bundling by dynein motors. This leads to an apparently isotropic contraction, and we proposed a continuum model [7], which quantitatively reproduced the experimental results. Crucially, the model helped explain why networks contract to a preferred final density regardless of sample geometry and motor concentration. The continuum model assumed that the active material stress tensors were isotropic and of the form $f(\rho)\boldsymbol{I}$, with $f < 0$ a combination of contractile motor stresses and repulsive steric stresses.

Here, we explore the same system as in our previous work [7] further by varying the initial MT density and the length distribution of MTs and measuring the resulting effects on the contraction process. Consistent with the predictions of our active fluid model, we find that the final network density varies little across a wide range of conditions. Intriguingly, we also find a correlation between the timescale of the contraction process and the average length of MTs in the system. To gain insight into how this microscopic parameter influences the macroscopic contraction timescale, we developed simulations of the contraction process. These simulations recapitulate many key aspects of the experimental results, including the variation of contraction timescale with MT length, and allow access to many aspects of the system difficult to measure experimentally, such as the spatial distribution and nature of the material stress tensors. Taken together, these results further support the underlying assumptions and key predictions of our active fluid model, and provide a framework for future studies.

2. Methods

2.1. Preparation of *Xenopus* extracts
Extracts were prepared from freshly laid *Xenopus* oocytes as described previously [20]. Fresh extracts were sequentially filtered through 2.0, 1.2, and 0.2 μm filters before being flash frozen in liquid nitrogen and stored at $-80\,^{\circ}$C until use.

2.2. Preparation of microfluidic devices
Microfluidic device templates were designed using AutoCAD 360 and Silhouette Studio software. Device templates were cut from 125 μm tape (3M Scotchcal) using a Silhouette Cameo die cutter, and adhered to petri dishes to create a master. PDMS (Sylgard 184, Dow Corning) was mixed at the standard 10:1 ratio, poured onto masters, degassed under vacuum, and cured overnight at 60 $^{\circ}$C. The cured devices were then removed from the masters and inlets and outlets were created using biopsy punches. Devices and coverslips were treated with air plasma using a corona device, bonded, and loaded with passivation mix composed of 5 mg ml^{-1} BSA and 2.5% (w/v) Pluronic F-127 before overnight incubation at 12 $^{\circ}$C.

2.3. Bulk contraction assay
The bulk contraction assay was performed as previously described [7]. Briefly, Alexa-647 labeled tubulin was added to 20 μL *Xenopus* extract at a final concentration of $\approx 1\,\mu$M. Then, 0.5 μL of taxol suspended in DMSO was then added to the extract to the indicated final concentration. Extracts were then loaded into passivated microfluidic devices, sealed with vacuum grease, and imaged using spinning disk confocal microscopy (Nikon TE2000-E microscope, Yokugawa CSU-X1 spinning disk, Hamamatsu ImagEM camera, 2× objective, Metamorph acquisition software). The time $t = 0$ corresponds to when imaging begins, typically <1 min after taxol addition. Images were analyzed using ImageJ and custom MATLAB software. The $\epsilon(t)$ curves were fit using time points when $\epsilon(t) > 0.1$.

2.4. Initial and final density estimation
In order to estimate network densities, we first assume that Alexa-647 labeled tubulin uniformly incorporates into MTs, and the overall concentration of tubulin is taken to be constant and equal to the previously measured value of 18 μM [21]. From this we can take,

$$18\,\mu\mathrm{M} = \frac{\sum_{i=1}^{N} M_i}{\sum_{i=1}^{N} V_i} = \frac{\sum_{i=1}^{N} \beta I_i(\ell A)}{\sum_{i=1}^{N} \ell A} = \beta \langle I \rangle_N,$$

where M_i is the tubulin mass in pixel i, β is a constant conversion factor between concentration in micromolar and fluorescence intensity, ℓ is the depth of the sample, A is the area of the pixel, $V_i = \ell A$ is the volume

corresponding to pixel i, N is the total number of pixels, I_i is the measured intensity of pixel i, A is the area of pixel i, and $\langle I \rangle_N$ is the measured intensity averaged over all pixels in the channel. From this we can infer,

$$\beta = \frac{18 \, \mu M}{\langle I \rangle_N}.$$

The intensity at each pixel in the network contains a contribution N_i from polymerized tubulin and a contribution B_i from monomeric, unpolymerized tubulin. The signal from monomeric tubulin is assumed to be constant and homogeneous throughout the channel. Thus, at the given time point where the background and network intensities are measured, the average concentration of polymerized tubulin in the network is given by,

$$\langle \rho \rangle (t) = \frac{\beta}{N_{network}} \sum_{i=1}^{N_{network}} N_i = \frac{\beta}{N_{network}} \sum_{i=1}^{N_{network}} [I_i - B],$$

$$= \beta [\langle I \rangle_{network} - B] = 18 \, \mu M \frac{\langle I \rangle_{network} - B}{\langle I \rangle_N},$$

where $N_{network}$ is the number of pixels in the network at the time point, and $\langle I \rangle_{network}$ is the intensity averaged over all pixels in the network.

To estimate the network density, the frame at the time closest to $t = T_c + \tau$ was selected, where τ is the characteristic contraction time and T_c is the lag time between the beginning of imaging and the beginning of network contraction [7]. This frame was corrected for inhomogeneous illumination and the camera's dark current, and analyzed as above to find $\langle \rho \rangle (T_c + \tau)$. As we assume that no MTs are created, destroyed, or added to the network during the contraction process, the total mass of MTs in the network must be conserved. Thus,

$$M_{network} = \langle \rho \rangle_0 V_0 = \langle \rho \rangle (t = T_c + \tau) V_{T_c + \tau} = \langle \rho \rangle_F V_F,$$

where V_0, $V_{T_c + \tau}$, V_F are the volume of the network at the beginning, at time $T_c + \tau$, and at the final state. Then,

$$\langle \rho \rangle (0) = \langle \rho \rangle (T_c + \tau) \frac{V_{T_c + \tau}}{V_0} = \langle \rho \rangle (T_c + \tau) \frac{W_{T_c + \tau} H_{T_c + \tau} L_{T_c + \tau}}{W_0 H_0 L_0},$$

where W, H, L are the width, height and length of the network at different times, denoted by the subscripts as with the volume. We assume that, as the network is pinned at the channel's inlet and outlet, there is no change in volume along the channel's length, and thus $L_0 = L_{T_c + \tau}$. Combining equations (1) and (2) in results,

$$\epsilon (t = T_c + \tau) = \epsilon_\infty (1 - e^{-1}) = \frac{W_0 - W(t = T_c + \tau)}{W_0} = 1 - \frac{W_{T_c + \tau}}{W_0},$$

which simplifies to,

$$\frac{W_{T_c + \tau}}{W_0} = 1 - \epsilon_\infty (1 - e^{-1}).$$

We further assume that the change in the network's height follows the same functional form as the change in width and thus,
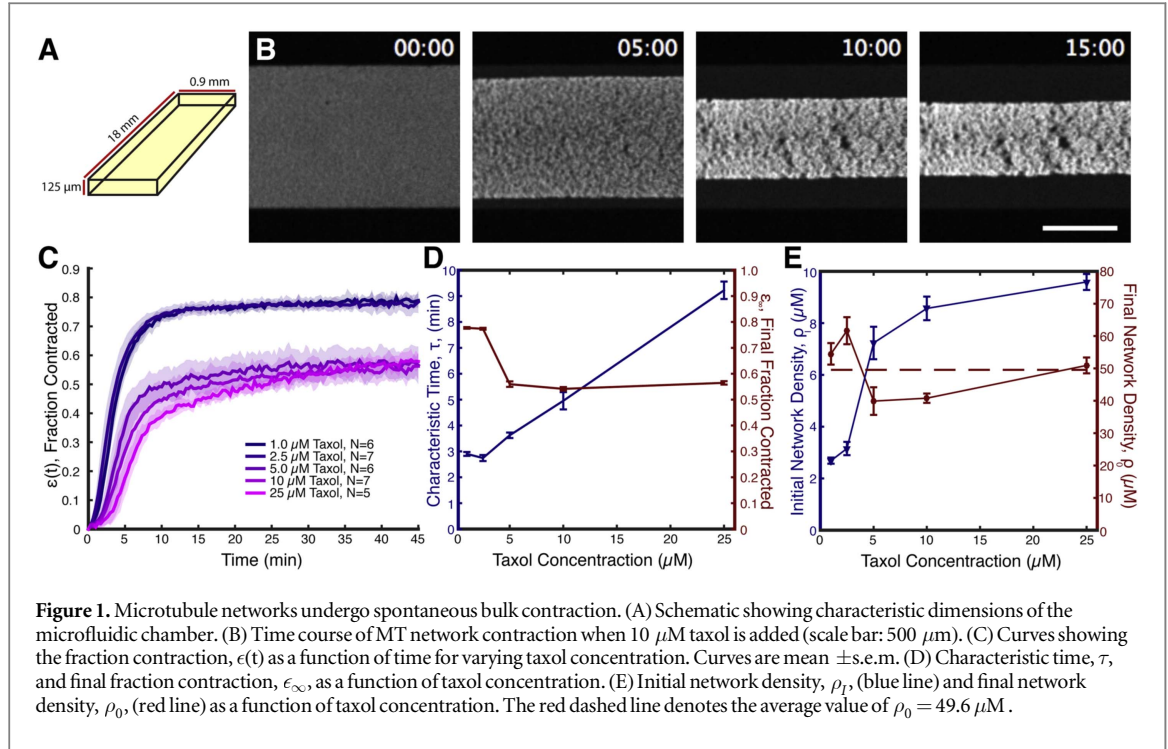
$$\langle \rho \rangle (0) = \langle \rho \rangle (T_c + \tau)[1 - \epsilon_\infty (1 - e^{-1})]^2.$$

For the final density of the network, similar reasoning can be used to show,

$$\langle \rho \rangle_F = \frac{1}{(1 - \epsilon_\infty)^2} \langle \rho \rangle_0 = \frac{[1 - \epsilon_\infty (1 - e^{-1})]^2}{(1 - \epsilon_\infty)^2} \langle \rho \rangle (T_c + \tau).$$

2.5. Measurement of MT length distributions

Stabilized MTs were dissociated from motor proteins and fixed as previously described [22]. MTs were allowed to assemble at room temperature for 30 min (unless otherwise noted) before 5 μl of extract was diluted into 50 μl of MT dissociation buffer (250 mM NaCl, 10 mM K-HEPES, pH 7.7, 1 mM $MgCl_2$, 1 mM EGTA, and 20 μM taxol). After a 2 min incubation, 100 μl of Fix Buffer (0.1% glutaraldehyde in 60% glycerol, 40% BRB80) was added and incubated for 5 min. 1 ml of Dilution Buffer (60% glycerol, 40% BRB80) was added to dilute the sample, and 2 μl of the diluted sample was spread between a slide and a 22 $\times$ 22 mm^2 coverslip. After waiting 30 min to allow the MTs to adhere to the coverslip, MTs were imaged using spinning disk confocal microscopy (Nikon TE2000-E microscope, Yokugawa CSU-X1 spinning disk, Hamamatsu ImagEM camera, 60$\times$ objective, Metamorph acquisition software). Active contours were fit to individual MTs using the ImageJ plugin JFilament [23], and MT lengths were determined from the contours using custom MATLAB software. For each taxol concentration, distributions of MT lengths were fit to a log-normal distribution to find the location parameter, μ, and the scale parameter, σ. In each case, the mode microtubule length for the log-normal distribution is given by

Figure 1. Microtubule networks undergo spontaneous bulk contraction. (A) Schematic showing characteristic dimensions of the microfluidic chamber. (B) Time course of MT network contraction when 10 μM taxol is added (scale bar: 500 μm). (C) Curves showing the fraction contraction, $\epsilon(t)$ as a function of time for varying taxol concentration. Curves are mean $\pm$ s.e.m. (D) Characteristic time, τ, and final fraction contraction, ϵ_∞, as a function of taxol concentration. (E) Initial network density, ρ_I, (blue line) and final network density, ρ_0, (red line) as a function of taxol concentration. The red dashed line denotes the average value of $\rho_0 = 49.6\,\mu$M.

$$l_{\text{mode}} = e^{\mu - \sigma^2}.$$

3. Results

To further investigate the dynamics of contracting MT networks in *Xenopus* oocyte extracts, we added taxol to the extracts to stabilize MTs, as previously described [7]. Extracts were loaded into rectangular microfluidic devices (figure 1(A)), sealed at the inlet and outlet using vacuum grease to prevent evaporation, and imaged at low magnification (methods). Within minutes of taxol addition, the MT networks were found to undergo a spontaneous bulk contraction as shown in our previous work [7] (figure 1(B), movie 1 available online at stacks. iop.org/NJP/19/125011/mmedia). The size of the network along the width of the channel, $W(t)$, was measured by identifying the pixels with high intensity (belonging to the network) and recorded as a function of time. Then the fraction contracted $\epsilon(t)$ was calculated, defined as
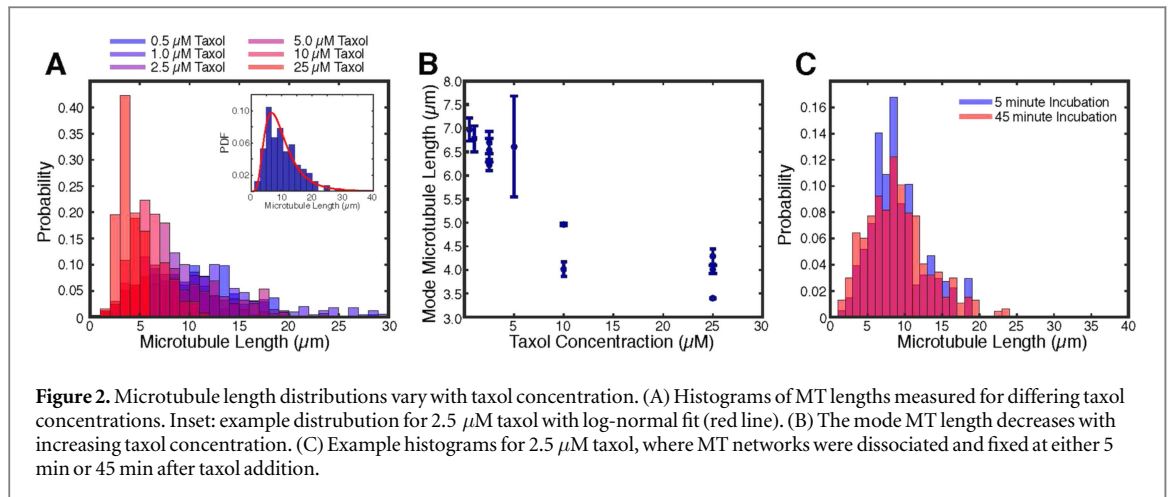
$$\epsilon(t) = \frac{W_0 - W(t)}{W_0}, \tag{1}$$

where W_0 is the width of the channel, typically 0.9 mm. This process was repeated for varying final concentrations of taxol, and the $\epsilon(t)$ curves for each taxol condition were averaged together to produce master curves for each condition (figure 1(C)). The $\epsilon(t)$ curves were well fit by a saturating exponential function,

$$\epsilon(t) = \epsilon_\infty [1 - e^{-\left(\frac{t - T_c}{\tau}\right)}], \tag{2}$$

where ϵ_∞ is the final fraction contracted, τ is the characteristic contraction time, and T_c is a lag time between the beginning of imaging and the beginning of the the contraction process. Equation (2) was fit to the $\epsilon(t)$ curves for each experiment to extract values for the characteristic time, τ, and the final fraction contracted, ϵ_∞. Values of τ and ϵ_∞ were averaged for each taxol condition (figure 1(D)). The characteristic timescale, τ, was found to increase with approximate linearity for taxol concentrations $> 2.5\,\mu$M, while the final fraction contracted, ϵ_∞, decreased slightly with increasing taxol concentration.

We next investigated how changing taxol concentration influenced both the initial density of the MT network, ρ_I, and the final density of the MT network, ρ_0. In systems of purified tubulin, the concentration of tubulin polymerized into MTs has been shown to increase with increasing taxol concentration [24]. Fluorescence intensity was used as a proxy for tubulin concentration, and was calibrated using previously measured values for the total tubulin concentration in *Xenopus* extracts (methods). While the initial density of the MT network, ρ_I, monotonically increased with increasing taxol concentration, the final density of the MT network displayed no obvious trend (figure 1(E)), and values of the final network density vary from the mean final density of $\rho_0 = 49.6\,\mu$M by less than 25%. This is consistent with previous results arguing that contracting MT networks in *Xenopus* extracts contract to a

Figure 2. Microtubule length distributions vary with taxol concentration. (A) Histograms of MT lengths measured for differing taxol concentrations. Inset: example distrubution for 2.5 μM taxol with log-normal fit (red line). (B) The mode MT length decreases with increasing taxol concentration. (C) Example histograms for 2.5 μM taxol, where MT networks were dissociated and fixed at either 5 min or 45 min after taxol addition.

preferred final density [7]. Also, the increase of initial MT density, ρ_I, with increasing taxol concentration appears to saturate for large taxol concentrations. Considering the three largest taxol concentrations investigated here (5, 10, and 25 μM), the initial MT densities was found to vary from the mean value by only 14% (std/mean), far less than the $\approx 2.5\times$ increase seen in the characteristic contraction timescale, τ, over this same range. Thus, τ does not scale proportionally to the initial density of MTs, ρ_I, and the change in contraction timescale must come from some other effect of changing taxol concentration.

Previously, it has been shown in clarified *Xenopus* extracts that the size of motor-organized taxol-stabilized MT assemblies, termed 'pineapples', decreased with increasing taxol concentration, presumably due to a decrease in the average length of MTs [22]. Thus, we next sought to measure the length distribution of MTs in our system for varying taxol concentrations. We used a previously described method to dissociate and fix MTs [22] (methods). Briefly, MTs were allowed to assemble for 5 min after taxol addition before being diluted into a dissociation buffer containing 250 mM NaCl, which dissociates motor proteins and other MAPs from the MTs. After a 2 min incubation, this mix was diluted again into a fixation buffer containing glutaraldehyde. MTs were fixed for 5 min, further diluted, and thinly spread between a slide and a 22 mm^2 coverslip. MTs were allowed to adhere for 30 min before imaging. An active contour was fit to MTs in the images [23], and the length of the active contour was used as a measure for the MT length. This process was repeated for each taxol concentration.

Example histograms of MT lengths for each taxol concentration are shown in figure 2(A). Visually, the peak of the distribution shifts towards smaller values of MT length for increasing taxol concentration. Empirically, we find that the distributions of MT lengths are well fit by a log-normal distribution (figure 2(A), inset). As fitting log-normal distributions to the measured histograms allows a more robust estimate of the mode MT length than using a purely empirical estimate, we fit the MT length distributions for each taxol concentration in order to find μ and σ, the two parameters of the log-normal distribution, and used these parameters to estimate the mode MT length for each condition. The mode MT length was found to decrease with increasing taxol concentration, varying by a factor of ≈ 1.7 across the taxol conditions measured (figure 2(B)).

One potential concern is that the MT length distribution may vary over the 45 min timescale of the contraction experiments. Potentially, this could be due to a number of factors, including MT depolymerization, severing of MTs, or other causes. To address this issue, we repeated our length distribution measurement where MT dissociation and fixation began 45 min after taxol addition. We find close agreement between the MT length distributions measured either 5 min or 45 min after taxol is added, indicating that the length distribution is approximately constant over the timescale of the contraction experiments (figure 2(C)).

4. Model and simulation

Our experimental results suggest that the change in contraction timescale observed for changing taxol concentrations may be due to changes in the MT length distribution. While our earlier continuum active gel theory for MT network contractions [7] captures the global contractile behavior of the network accurately, understanding the dependence of its parameters on microscale properties, such as MT length, is beyond the scope of the model. To resolve microscale changes and study their effects on the network's emergent properties, and to test the dependence of contraction timescale on MT lengths, we turn to simulation. Our simulation tracks the behavior of a suspension of fixed length MTs actuated by dynein motors which actively crosslink them and drag them through the fluid.

4.1. Model description

In our modeling, we represent MTs as rigid spherocylinders that interact sterically and through motor protein coupling. In principle the fluid in which MTs are suspended couples their dynamics globally. Since solving the full Stokes problem numerically is prohibitively expensive we here neglect hydrodynamic many-body couplings. Instead we approximate the effects of the fluid by a local drag, that is, each MT acts as if it moved through a quiescent fluid. Note that for a dense and highly percolated network, one expects long range hydrodynamic interactions to be screened and hence we argue that they can be safely ignored for our purposes.

Suspensions of passive Brownian spherocylinders are well understood in both theory and simulation, and our numerical framework (in appendix A) is based on well-known work [25–27]. What sets our simulations apart from the previous work is the presence of motor proteins, which have been previously considered with other simulation tools [28]. We model dynein motors as having a non-moving, fixed crosslinking end and a moving crosslinking end with stochastic binding and unbinding behaviors. The two ends are assumed to be connected by a Hookean spring with a rest length $l_D^0 \simeq 40$ nm, which is the size of a force-free dynein. Collisions amongst dyneins or between dyneins and MTs are ignored for simplicity. In our model, dyneins have one fixed end, which stays rigidly attached to one MT throughout the simulation, and one motor end which stochastically binds, unbinds, and walks along other MTs. The fixed end represents the p150 subunit of the dynactin complex, which contains a non-motor microtubule binding domain which attaches to microtubules [29, 30]. When the motor end is free, the dynein is transported with the MT bound to its fixed end without applying any force to it. Given the motor's small size, the orientation of such a motor is dominated by Brownian motion, i.e. is random. If a free motor head is closer than a characteristic capture radius r_{cap} to another MT, it binds with a probability $P_b = \Delta t/\tau_b$, where Δt is the time step size, and τ_b is the characteristic binding time. Should a free end be close enough to several MTs to bind them, its total binding probability P_b stays the same, and one of the candidate MTs is chosen randomly. Finally, for the binding location we choose the perpendicular projection of the dynein center onto the target MT. Bound motor ends walk towards the minus end of the MT they bind to, and exert a spring force and torque ($\boldsymbol{F}^{motor} = \kappa_D(l_D - l_D^0)\boldsymbol{e}_D$, $\boldsymbol{T}^{motor} = \boldsymbol{r}_D \times \boldsymbol{F}^{motor}$), where l_D, κ_D are the dynein's current length and its spring constant, respectively, $\boldsymbol{e}_D$ is the direction of the Hookean spring force along the direction of dynein, and $\boldsymbol{r}_D$ is a vector pointing from the center of mass of a MT to the point where the dynein binds and applies a Hookean spring force. Consistent with earlier work we impose a force velocity relation relation [13] and set the velocity

$$v = v_M(1 - \min(F^{motor}/F^{stall}, 1)) \text{ iff } F^{motor} < F^{stall} \tag{3}$$

and $v = 0$, otherwise. Here, v_M and F^{stall} are the motors free velocity and stall forces, respectively.

All bound motor ends can stochastically unbind, with a characteristic time

$$\tau_u = \tau_u^0 \exp\left(-F^{motor}/(F^{stall} - F^{motor})\right), \tag{4}$$

which becomes $\simeq \exp(-F^{motor}/F^{stall})$ for $F^{motor} \ll F^{stall}$, see [31], and diverges for $F^{motor} \to F^{stall}$. Here τ_u^0 is the force-free unbinding time. Finally, dyneins that reach the minus end do not immediately detach, but remain at the minus end, i.e. $v = 0$, keeping the same unbinding frequency.
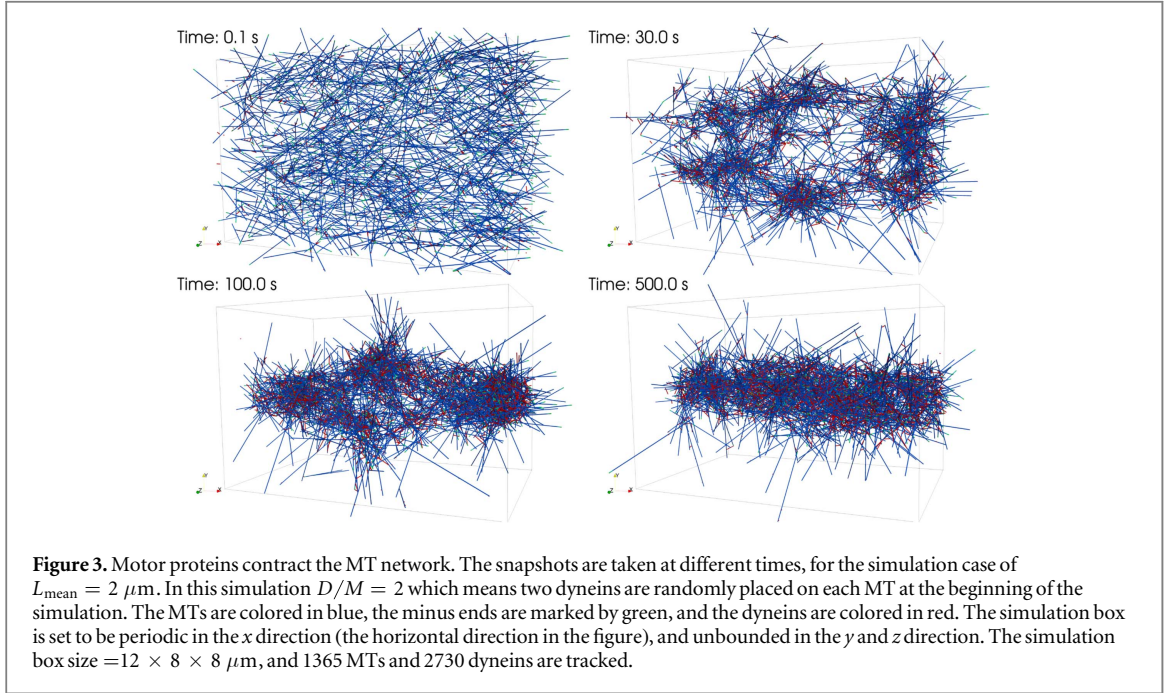
4.2. Setup and parameters

For this work we explored how key aspects of the microscopic model change the emergent behavior of the network. In particular, we varied the number of dyneins affixed to each MT, D/M, and the length distribution of MTs.

The full model has a large number of parameters. However, many can be fixed from estimates in the literature. We summarize in table 1 the parameters that are kept unchanged throughout the simulations presented here. We also fix the number of MTs in our simulations to be 10 μM, which is the approximate initial concentration found in experiments with 5–25 μM of taxol. Following the experimental results, the MT length distribution is taken to be lognormal with parameters (μ, σ), with σ fixed at 0.5. Note that in simulation we use shorter MTs than in the experiments due to limitations in computational resources, see appendix D.

In the simulations presented here, each MT carries the same number, D/M, of fixed dynein molecules, attached at random locations on the MT that carries them. Note that this is different from the assumptions made in earlier work [7], which has dyneins all fixed to the minus ends of MTs. This difference is motivated by the numerical observation that networks with all dyneins at minus ends will precipitate into asters, while networks with dyneins randomly affixed to MTs are more percolated and globally contract. It is unclear whether this difference between experimental results and the simulations presented here is due to experimental complexity not fully captured in the current simulations. Further exploring the effects of motor localization on the dynamics and organization of microtubule networks is a future research direction.

Table 1. The parameters fixed in simulations.

Parameter	Explanation	Value	Reference
l_{D}^0	Dynein free length	40 nm	Estimation
F^{stall}	Dynein stall force	1 pN	Estimation [31]
κ_{D}	Dynein spring constant	1 pN μm^{-1}	Estimation [32]
r_{cap}	Dynein capture radius	80 nm $= 2l_{\mathrm{D}}^0$	Assumption
v_M	Dynein max walking velocity	1 μm s^{-1}	Estimation [33]
τ_b	Dynein binding timescale	10^{-3} s	Assumed to be short
τ_u^0	Dynein unbinding timescale	10 s	Estimation [17, 33]
η	Fluid viscosity	0.02 pN μm^{-2} s^{-1}	Estimation [34]
k_{BT}	Energy scale at 300 K	4.11×10^{-3} pN μm	300 K

Figure 3. Motor proteins contract the MT network. The snapshots are taken at different times, for the simulation case of $L_{\mathrm{mean}} = 2$ μm. In this simulation $D/M = 2$ which means two dyneins are randomly placed on each MT at the beginning of the simulation. The MTs are colored in blue, the minus ends are marked by green, and the dyneins are colored in red. The simulation box is set to be periodic in the x direction (the horizontal direction in the figure), and unbounded in the y and z direction. The simulation box size $= 12 \times 8 \times 8$ μm, and 1365 MTs and 2730 dyneins are tracked.

All of our simulations are performed in a simulation box of size $12 \times 8 \times 8$ μm, with periodic boundary conditions along the long direction, mimicking the experimental geometry. The initial state is a random arrangement of MTs, in which all dynein motor ends are unbound.

4.3. Simulation results

Figure 3 shows a representative example of the numerically observed contractions. After an initial phase of $\simeq 30$ s, in which MTs locally rearrange and cluster, bulk contraction driven by dyneins begins. It takes ~ 100 s to create a single, fully percolated network. The system has approached a steady state at $\simeq 500$ s, where the network has contracted to a cylindrical ribbon along the periodic direction of the simulation box.

To compare the simulations to experiments, we calculate the fraction contracted

$$\epsilon(t) = \frac{R_0 - R(t)}{R_0}, \tag{5}$$

from our simulations. Here, $R(t)$ is the radius of a cylinder aligned with the periodic direction, and centered around the MT center of mass of the system portion which contains 50% of the total MT mass. By fitting $\epsilon(t)$ to the saturation exponential, e.g. equation (2), we now obtain a contraction timescale τ, and a final fraction contracted ϵ_∞, which can be directly compared to experiments. As was done for fitting the experimental results, we ignore the very early stages of contraction ($\epsilon(t) < 0.1$), since they mostly mirror the initial rearrangement of the network and not the global contraction dynamics.

Earlier work [7] has shown that τ depends on the initial system size. Since our numerical system is far smaller than the experimental one, we do not expect τ to quantitatively match experiments, but only to reproduce trends with varying parameters. Using the parameters from [7] which were measured by fitting a functional form to the characteristic timescale versus initial system width curves for systems with 2.5 μM taxol, and a system size of 8 μm, we expect a contraction time of $\tau \approx 90$ s, which is close to the time scales on which our numerical system contracts.
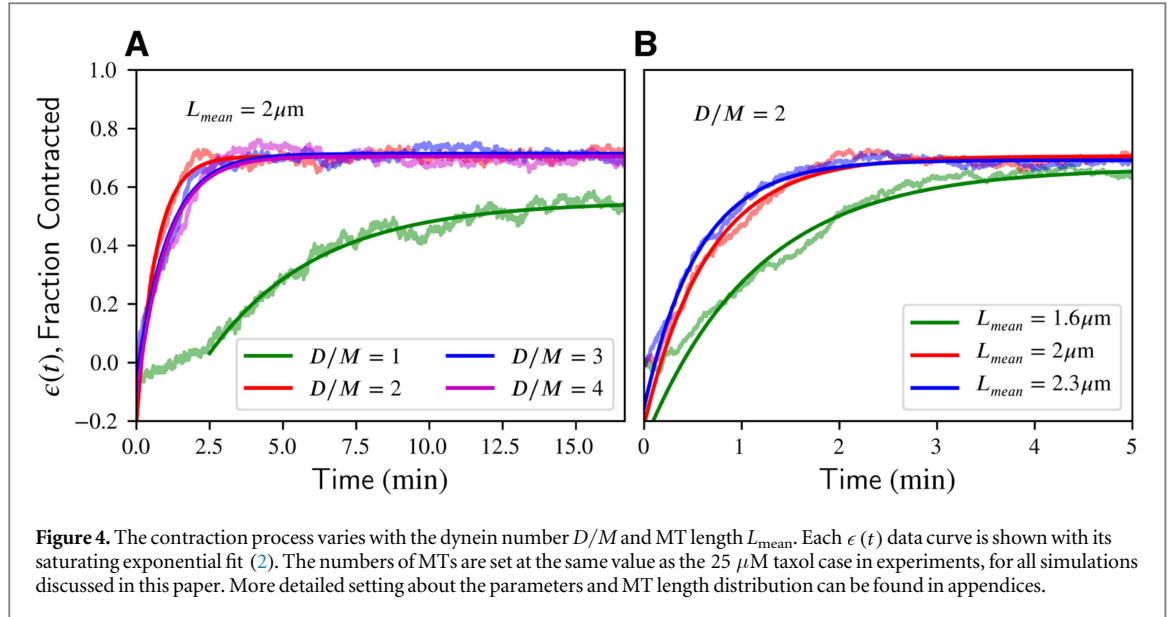
Figure 4. The contraction process varies with the dynein number D/M and MT length L_{mean}. Each $\epsilon(t)$ data curve is shown with its saturating exponential fit (2). The numbers of MTs are set at the same value as the 25 μM taxol case in experiments, for all simulations discussed in this paper. More detailed setting about the parameters and MT length distribution can be found in appendices.

Table 2. The fitted characteristic contraction time τ for different lengths of MTs at $D/M = 2$. All simulations start from the same network density as the one shown in figure 3.

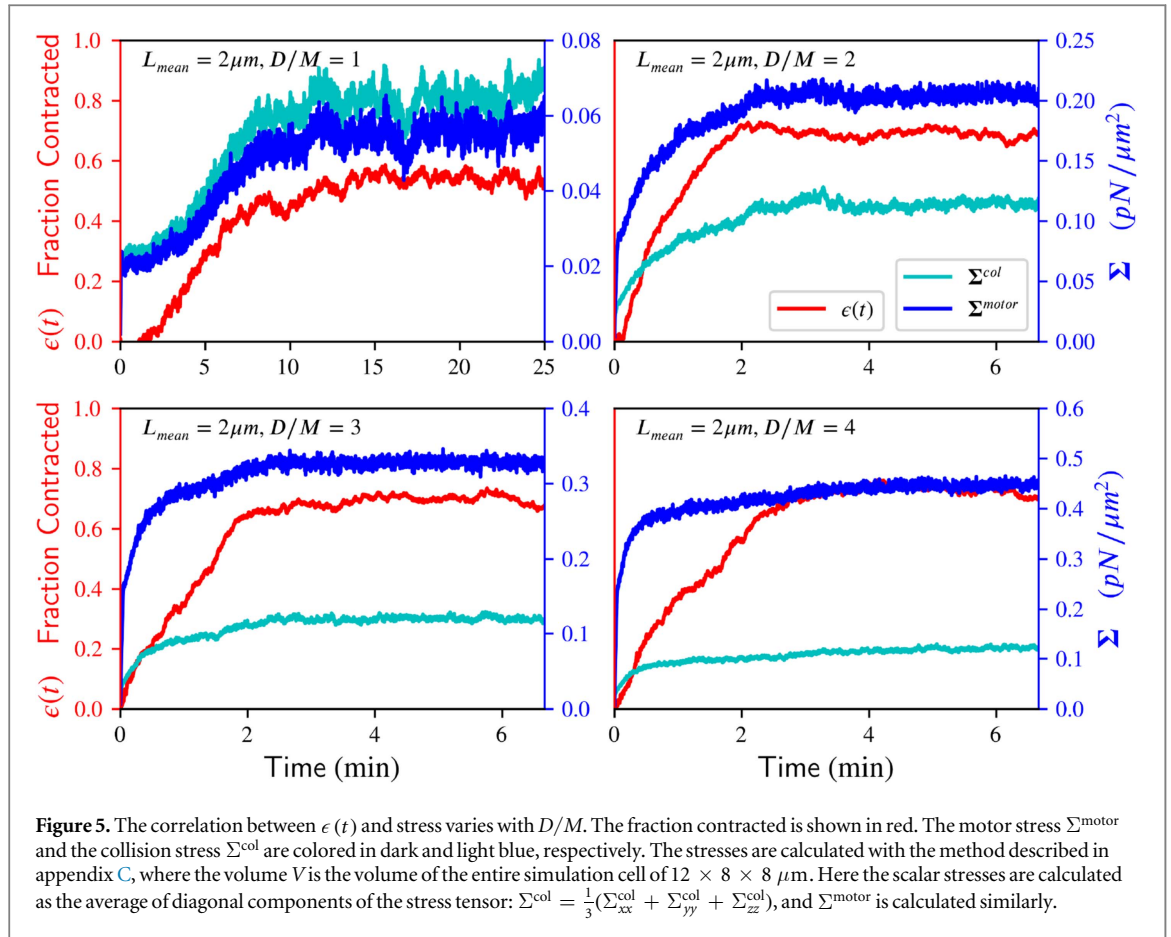| L_{mean} (μm)	1.618	2.007	2.297	2.511
τ (s)	68.6	39.4	33.4	28.8

The final fraction contracted, ϵ_∞, is easier to directly compare between experiments and simulation, since it does not depend on system size. Encouragingly, for the case of $D/M = 1$, the simulated contraction produces a similar final fraction contracted of $\epsilon_\infty \approx 0.55$, as in experiment, (figure 1(D) and figure 4). Note that here only taxol concentrations of 5, 10, 25 μM should be directly compared since the other conditions change the initial density of the system to values which differ significantly from our simulations.

To further test our numerical model, we investigated how the contraction timescale varies with the number of motors in the system. As expected from [7], increasing D/M to 2 drastically changes the contraction timescale, with only minor changes in ϵ_∞ (figure 4(A)). Further increasing D/M does not significantly change either the timescale τ, or the final fraction ϵ_∞. We also tested whether our model can reproduce the changes of contraction times for different length distributions of MTs, corresponding to different taxol concentrations, as seen in experiment. Indeed, as the mean length of MTs is increased, the contractions speed up (figure 4(B), table 2), yet the final fraction contracted does not change significantly. This is again consistent with experimental results, (figure 1). We conclude that our simulations are consistent with key features of the experiments.

Having gained confidence in our simulation tools, we next inspect important aspects of the physics of the MT network which are experimentally difficult to access. We first ask how the system stress changes during the contraction process. We extract the stress from our simulations using the expressions detailed in appendix C. In particular, we can distinguish between the stress tensor contributions from steric collisions, $\mathbf{\Sigma}^{\text{col}}$, and the active stress tensor generated by motors, $\mathbf{\Sigma}^{\text{motor}}$.

Figure 5 shows $\mathbf{\Sigma}^{\text{col}}$, $\mathbf{\Sigma}^{\text{motor}}$, and $\epsilon(t)$, for $L_{\text{mean}} = 2$ μm and different numbers of D/M, as a function of time. From this data, we make four key observations. First, we observed that the average stress tensors $\mathbf{\Sigma}^{\text{col}}$ and $\mathbf{\Sigma}^{\text{motor}}$ are dominated by their diagonal components, and the three diagonal components are within $\sim 20\%$ of each other. We report in figure 5 the average of the trace of the stress tensor: $\Sigma^{\text{col}} = \frac{1}{3}(\Sigma_{xx}^{\text{col}} + \Sigma_{yy}^{\text{col}} + \Sigma_{zz}^{\text{col}})$, and Σ^{motor} is calculated similarly. Second, we find that at low D/M, i.e. 1 or 2, the growth of $\epsilon(t)$ and of both stress contributions occur on the same timescale. This breaks down at larger D/M for which the stresses grow and saturate much faster than $\epsilon(t)$. Third, increasing D/M leads to increasing $\mathbf{\Sigma}^{\text{motor}}$, while $\mathbf{\Sigma}^{\text{col}}$ rapidly saturates. Fourth, as $\mathbf{\Sigma}^{\text{col}}$ saturates, the overall contraction timescale ceases to decrease (see also figure 4). These observations point to the local structure formation changing significantly for larger D/M, which we further explore.

Figure 6 shows the spatial distribution of MT volume fraction, motor stress, and collision stress for the $D/M = 2$ and 4 cases. At 60 s with $D/M = 4$, the MTs are quickly dragged by dyneins into dense local clusters while the
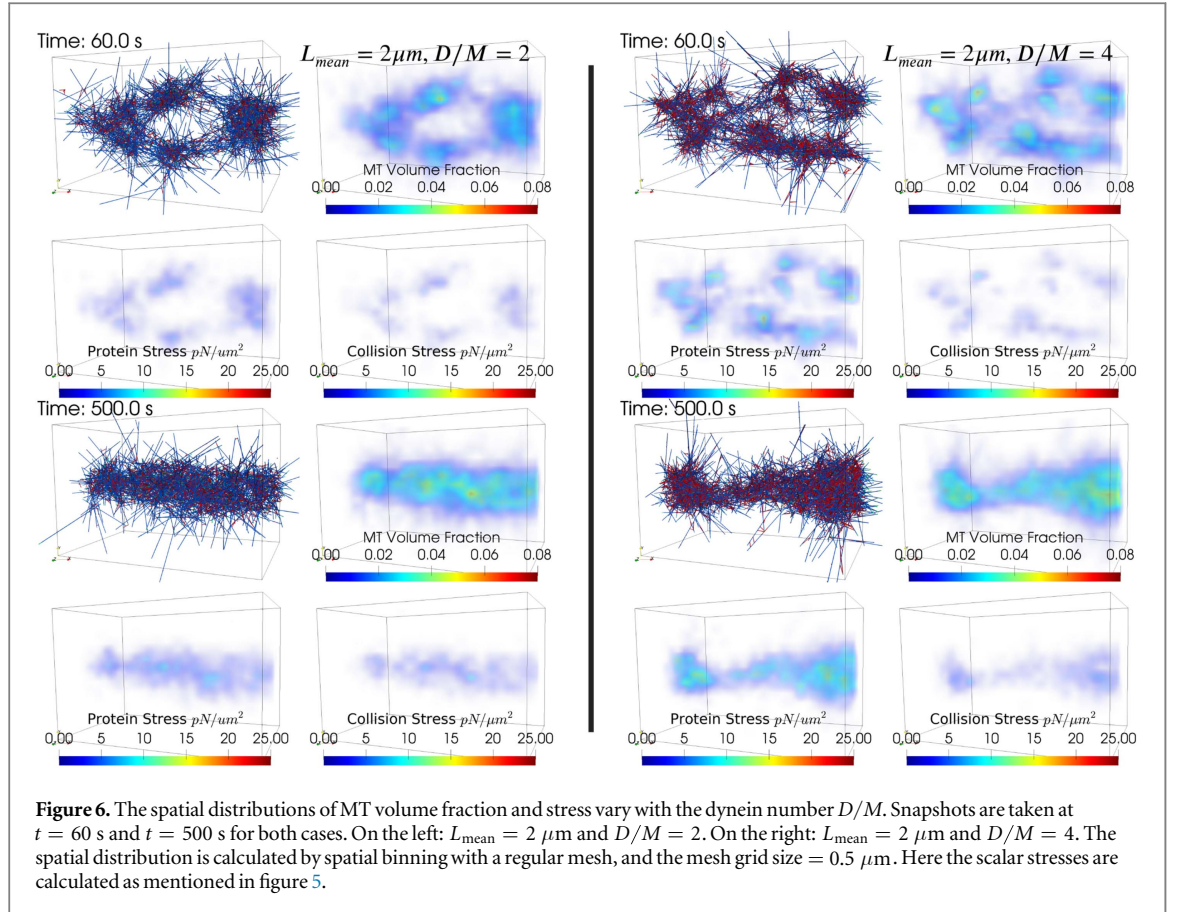
Figure 5. The correlation between $\epsilon(t)$ and stress varies with D/M. The fraction contracted is shown in red. The motor stress Σ^{motor} and the collision stress Σ^{col} are colored in dark and light blue, respectively. The stresses are calculated with the method described in appendix C, where the volume V is the volume of the entire simulation cell of $12 \times 8 \times 8\ \mu m$. Here the scalar stresses are calculated as the average of diagonal components of the stress tensor: $\Sigma^{col} = \frac{1}{3}(\Sigma^{col}_{xx} + \Sigma^{col}_{yy} + \Sigma^{col}_{zz})$, and Σ^{motor} is calculated similarly.

clusters have not contracted much toward the center. At this stage, Σ^{col} and Σ^{motor} have significantly increased but $\epsilon(t)$ remains low. In contrast, for $D/M = 2$ the distibution at $t = 60$ s is much less clustered. Consistently for $D/M \leqslant 2$ the growth of Σ^{col} and Σ^{motor} is more synchronized with $\epsilon(t)$. This observation suggests a possible continuum model to predict the behavior of the entire network based on an 'equation-of-state' relating the local microscopic parameters and the binding-walking-unbinding cycles of dyneins to the local mechanical stress tensors Σ^{col} and Σ^{motor}, as the driving 'force' of the contraction, which will be the subject of future work.

5. Discussion

Here we examined how the dynamics of bulk MT network contraction in *Xenopus* extracts vary with taxol concentration. We find that using different taxol concentrations, the networks contract to approximately the same final density, even though the initial density of the networks varies by a factor of ≈3.6. While the final density of these networks is constant, we find that the timescale of the contraction process increases with increasing taxol concentration. In the high taxol regime, where the initial network density varies by only ≈14%, we find that the timescale increases by a factor of ≈2.5, arguing that the timescale is not simply varying proportionally to the initial network density. The length distributions of the MTs were measured for each taxol condition, and it was found that the average MT length decreases with increasing taxol concentration by a factor of ≈1.7 across the tested conditions. We postulate that it is this change in MT length that drives the changes in contraction time, and turn to simulation to test this idea.

We built a simulation tool to reveal more microscopic information of the network contraction process, and found that by placing dyneins randomly on each MT, we could simulate a contraction process consistent with experiments. We found that the characteristic contraction timescale, τ, is decreased by increasing only the MT length, which is consistent with the experimental result that shorter MTs at higher taxol concentration contract slower. We also investigated the effect of dynein number on the contraction process. Increasing the number of dynein per MT, D/M, from 1 to 2 sped up the contraction significantly, but further increasing the dynein number did not affect the contraction. Instead, an increase of D/M generated a local clustering structure at the early stage of the contraction, and then the local clusters contract. This process is clearly revealed by the spatial-temporal variations of collision and motor stresses, and their correlation with the contraction process $\epsilon(t)$. This indicates that we could possibly build a microscopic 'equation-of-state' to improve our previous coarse-grained model [7] to directly relate the stress terms in the model with microscopic motor behaviors, which will be the focus of future work.

Figure 6. The spatial distributions of MT volume fraction and stress vary with the dynein number D/M. Snapshots are taken at $t = 60$ s and $t = 500$ s for both cases. On the left: $L_{\text{mean}} = 2\ \mu$m and $D/M = 2$. On the right: $L_{\text{mean}} = 2\ \mu$m and $D/M = 4$. The spatial distribution is calculated by spatial binning with a regular mesh, and the mesh grid size $= 0.5\ \mu$m. Here the scalar stresses are calculated as mentioned in figure 5.

Acknowledgments

Appendix A. Algorithm for MT network simulation

The simulation program tracks the motion of MTs driven by motor proteins by modeling MTs as rigid spherocylinders and motor proteins as Hookean springs with crosslinking ends. At this micron-sized scale the motion of objects in fluid is overdamped, and MTs are tracked with the following simple explicit Euler time stepping, where $\boldsymbol{X}_i$ is the center of mass and $\boldsymbol{q}_i$ is the unit orientation vector of MT i:

$$\Delta \boldsymbol{X}_i = \boldsymbol{M}_i \cdot (\boldsymbol{F}_i^{\text{motor}} + \boldsymbol{F}_i^{\text{col}})\Delta t + \Delta \boldsymbol{X}_i^B, \tag{A.1}$$

$$\Delta \boldsymbol{q}_i = \frac{1}{\gamma_i^R}(\boldsymbol{T}_i^{\text{motor}} + \boldsymbol{T}_i^{\text{col}}) \times \boldsymbol{q}_i \Delta t + \Delta \boldsymbol{q}_i^B. \tag{A.2}$$

The forces $\boldsymbol{F}^{\text{motor}}$ and $\boldsymbol{F}^{\text{col}}$ stem from motor proteins and collisions between MTs, respectively, with $\boldsymbol{T}^{\text{motor}}$ and $\boldsymbol{T}^{\text{col}}$ being the corresponding torques. Finally $\Delta \boldsymbol{X}^B$ and $\Delta \boldsymbol{q}^B$ are the Brownian contributions to the motion of MTs.

The mobility matrix $\boldsymbol{M}_i$ describes the effect of hydrodynamic drag. In principal all MTs are fully coupled through the Stokes equation, but in this work we ignore this coupling. Here, the $\boldsymbol{M}_i$ of each MT i is approximated as if each MT is moving individually by itself in unbounded fluid. $\boldsymbol{M}_i$ takes a 3×3 symmetric matrix form because we modeled each MT as an axisymmetric spherocylinder:

$$\boldsymbol{M}_i^{-1} = \gamma_i^{\parallel} \boldsymbol{q}_i \boldsymbol{q}_i + \gamma_i^{\perp}(\boldsymbol{I} - \boldsymbol{q}_i \boldsymbol{q}_i), \tag{A.3}$$

where $\boldsymbol{I}$ is the 3×3 identity matrix. $\gamma_i^{\parallel}$ and $\gamma_i^{\perp}$ are the translational drag coefficients for motions parallel and perpendicular to the axis of the MT i, depending on the fluid viscosity η, the MT length L_i, and the diameter D_i. Drags are solvable from the slender-body theory [35]:

$$\gamma_i^{\perp} = \frac{8\pi\eta L_i}{b_i + 2}, \quad \gamma_i^{\parallel} = \frac{8\pi\eta L_i}{2b_i}, \quad \gamma_i^r = \frac{2\pi\eta L_i^3}{3(b_i + 2)}, \tag{A.4}$$

where $b_i = -(1 + 2\ln(D_i/L_i))$ is a geometric parameter. For MTs we have $L_i \gg D_i$, and $b_i \approx 2\ln(L_i/D_i)$, and so we have $\gamma_i^{\perp} \approx 2\gamma_i^{\parallel}$. In simulations, we used the same diameter D for all MTs.

At each timestep the Brownian displacement and rotation $\Delta \boldsymbol{X}_i^B$ and $\Delta \boldsymbol{q}_i^B$ are generated as Gaussian random vectors. The means are zero, while the variances are given by the local fluctuation-dissipation relation:

$$\langle \Delta \boldsymbol{X}_i^B \Delta \boldsymbol{X}_i^B \rangle = 2k_B T \boldsymbol{M}_i \Delta t, \tag{A.5}$$

$$\langle \Delta \boldsymbol{q}_i^B \Delta \boldsymbol{q}_i^B \rangle = 2k_B T (\boldsymbol{I} - \boldsymbol{q}_i \boldsymbol{q}_i) \Delta t / \gamma_i^r. \tag{A.6}$$

We follow the method of Tao *et al* [36] to generate these two random vectors.

For equation (A.1), the motor force and torque are described in the main text. The collision force $\boldsymbol{F}_i^{col}$ and torque $\boldsymbol{T}_i^{col}$ are calculated in the simulation as detailed in appendix B.

Appendix B. Collision between microtubules

When two MTs i and j are close to each other, the shortest distance d_{ij} between their axes is calculated. If d_{ij} is smaller than the microtubule diameter D then a collision force $\boldsymbol{F}^{col}$ is calculated with a WCA-type repulsive force to prevent them from overlapping and crossing each other. The original WCA potential is stiff and poses a severe limit on the maximum timestep Δt in simulations. We used a softened WCA potential to enable larger timesteps:

$$d \geqslant \beta D: \quad F^{col}(d) = -24\left(\frac{k_B T}{D}\right)\left[\frac{1}{(\alpha + d/D)^7} - \frac{2}{(\alpha + d/D)^{13}}\right], \tag{B.1}$$

$$d < \beta D: \quad F_L^{col}(d) = F^{col}(\beta D) + \frac{\partial F^{col}}{\partial d}\Big|_{d=\beta D}(d - \beta D), \tag{B.2}$$

where $F^{col}(d)$ is a shifted WCA potential with a shift parameter α. For $\alpha = 0$, $F^{col}(d)$ becomes the usual WCA repulsive force. $F_L^{col}(d)$ is a linearized continuation of $F^{col}(d)$ for $d < \beta D$, to prevent the blow-up of collision force at small d. In simulations we fix $\alpha = 0.1$ and $\beta = 0.95$, to preserve the repulsion between MTs, but enable the simulations to complete within reasonable simulation time. Also due to the use of a soft repulsive force instead of an accurate rigid interaction, the effective diameter of MTs are estimated to be about $\sim$80% of the specified diameter D [36]. Therefore in simulations D is set to 30 nm to reproduce the true diameter 24 nm of MTs.

Appendix C. The calculation of stress and its spatial distribution

The stress can be calculated by the binding force and collision force in equation (A.1). Since both contributions are pairwise between MTs, and satisfy Newton's third law, we can calculate the stress tensor pair-by-pair with the virial theorem. Also, because the MTs are thin-and-long slender cylinders, the calculation can be further simplified [37].

For two MTs i and j, their contribution to the total system stress is a 3×3 tensor formed by the outer product:

$$\boldsymbol{\sigma}^{(i,j)} = -(\boldsymbol{x}^{(i)} - \boldsymbol{x}^{(j)})\boldsymbol{f}^{(i,j)}, \tag{C.1}$$

where $\boldsymbol{r}^{(ij)} = \boldsymbol{x}^{(i)} - \boldsymbol{x}^{(j)}$, is the vector pointing from the forcing location $\boldsymbol{x}^{(j)}$ on MT j to $\boldsymbol{x}^{(i)}$ on MT i. $\boldsymbol{f}^{(i,j)}$ is the force from j to i. For the collision force, $\boldsymbol{x}^{(i)}$ and $\boldsymbol{x}^{(j)}$ are the two collision points on each MT. For the dynein binding force, $\boldsymbol{x}^{(i)}$ and $\boldsymbol{x}^{(j)}$ are the two binding locations (two ends) of one dynein on the two MTs. If more than one dyneins bind i and j, the contribution from each dynein is calculated and added independtly.

Each $\boldsymbol{\sigma}^{(i,j)}$ contributes to the total system stress tensor at the spatial location $(\boldsymbol{x}^{(i)} + \boldsymbol{x}^{(j)})/2$, which is the center of the two forcing location. For a certain volume V in space, the average stress tensor in this volume is a simple arithmetic average of all $\boldsymbol{\sigma}^{(i,j)}$ in this volume:

$$\boldsymbol{\Sigma}_V^{col} = -\frac{1}{V}\sum_{\in V} \boldsymbol{\sigma}^{(i,j),col}, \quad \boldsymbol{\Sigma}_V^{motor} = -\frac{1}{V}\sum_{\in V} \boldsymbol{\sigma}^{(i,j),motor}. \tag{C.2}$$

Appendix D. The length distribution of microtubules

The length distribution of MTs is taken to be given by a lognormal distribution with parameters μ and σ:

$$P(L) = \frac{e^{-\frac{(\log(L)-\mu)^2}{2\sigma^2}}}{\sqrt{2\pi}L\sigma}, \quad L_{mean} = e^{\mu+\sigma^2/2}, \quad L_{mode} = e^{\mu-\sigma^2}. \tag{D.1}$$

Table D1. The settings of MT length in simulations.

e^{μ} (μm)	1.0	1.5	2.0	2.5	3.0
L_{mean} (μm)	1.123	1.618	2.007	2.297	2.511
L_{mode} (μm)	0.779	1.168	1.558	1.947	2.336

In the simulations, to detect the binding and collision events a nearest neighbor search procedure is performed during each timestep, and long MTs significantly slow down its efficiency. Also, due to the periodic boundary condition used in simulations, a MT with length of the simulation box size may interact with its own periodic image, and generates some unphysical results. Therefore in simulations the lognormal distribution is clipped at L_{max}, and the mean length of the MTs changes:

$$L_{mean} = \frac{e^{\mu + \frac{\sigma^2}{2}} \mathrm{Erfc}\left(\frac{\mu - \log(L_{max}) + \sigma^2}{\sqrt{2}\,\sigma}\right)}{\mathrm{Erfc}\left(\frac{\mu - \log(L_{max})}{\sqrt{2}\,\sigma}\right)}. \tag{D.2}$$

While the mode length does not change with L_{max}.

In simulations we used $L_{max} = 4$ μm, which is half of the width of a simulation box with size $12 \times 8 \times 8$ μm. We also fixed $\sigma = 0.5$ to match the experiment data, and the actual simulation settings are detailed in table D1.

ORCID iDs

Peter J Foster ⬤ https://orcid.org/0000-0003-1818-5886
Wen Yan ⬤ https://orcid.org/0000-0002-9189-0840

References

[1] Marchetti M C *et al* 2013 Hydrodynamics of soft active matter *Rev. Mod. Phys.* **85** 1143–89
[2] Prost J, Jülicher F and Joanny J F 2015 Active gel physics *Nat. Phys.* **11** 111–7
[3] Sanchez T, Chen D T N, DeCamp S J, Heymann M and Dogic Z 2012 Spontaneous motion in hierarchically assembled active matter *Nature* **491** 431–4
[4] Linsmeier I, Banerjee S, Oakes P W, Jung W, Kim T and Murrell M P 2016 Disordered actomyosin networks are sufficient to produce cooperative and telescopic contractility *Nat. Commun.* **7** 1–9
[5] Surrey T, Nédélec F, Leibler S and Karsenti E 2001 Physical properties determining self-organization of motors and microtubules *Science* **292** 1167–71
[6] Nédélec F J, Surrey T, Maggs A C and Leibler S 1997 Self-organization of microtubules and motors *Nature* **389** 305–8
[7] Foster P J, Fürthauer S, Shelley M J and Needleman D J 2015 Active contraction of microtubule networks *eLife* **4** e10837
[8] Brugués J and Needleman D 2014 Physical basis of spindle self-organization *Proc. Natl Acad. Sci. USA* **111** 18496–500
[9] Naganathan S R, Fürthauer S, Nishikawa M, Jülicher F and Grill S W 2014 Active torque generation by the actomyosin cell cortex drives left-right symmetry breaking *eLife* **3** e04165
[10] Mayer M, Depken M, Bois J S, Jülicher F and Grill S W 2010 Anisotropies in cortical tension reveal the physical basis of polarizing cortical flows *Nature* **467** 617–21
[11] Shelley M J 2016 *Annu. Rev. Fluid Mech.* **48** 487–506
[12] Sanchez T, Chen D, DeCamp S, Heymann M and Dogic Z 2012 Spontaneous motion in hierarchically assembled active matter *Nature* **491** 431–4
[13] Gao T, Blackwell R, Glaser M A, Betterton M D and Shelley M J 2015 *Phys. Rev. E* **92** 062709
[14] Belmonte J M, Leptin M and Nédélec F 2017 A theory that predicts behaviors of disordered cytoskeletal networks *Mol. Syst. Biol.* **13** 941
[15] Nédélec F and Surrey T 2001 Dynamics of microtubule aster formation by motor complexes *C. R. Acad. Sci.* IV **2** 841–7
[16] Hentrich C and Surrey T 2010 Microtubule organization by the antagonistic mitotic motors kinesin-5 and kinesin-14 *J. Cell Biol.* **189** 465–80
[17] Tan R, Foster P J, Needleman D J and McKenney R J 2017 Cooperative accumulation of dynein-dynactin at microtubule minus-ends drives microtubule network reorganization *bioRxiv* (https://doi.org/10.1101/140392)
[18] White D, Vries G, Martin J and Dawes A 2015 Microtubule patterning in the presence of moving motor proteins *J. Theor. Biol.* **382** 81–90
[19] Taunenbaum M E, Vale R D and McKenney R 2013 Cytoplasmic dynein crosslinks and slides anti-parallel microtubules using its two motor domains *eLife* **2** e00943
[20] Hannak E and Heald R 2006 Investigating mitotic spindle assembly and function *in vitro* using Xenopus laevis egg extracts *Nat. Protocols* **1** 2305–14
[21] Parsons S F and Salmon E D 1997 Microtubule assembly in clarified Xenopus egg extracts *Cell Motility Cytoskeleton* **36** 1–11
[22] Mitchison T J, Nguyen P, Coughlin M and Groen A C 2013 Self-organization of stabilized microtubules by both spindle and midzone mechanisms in Xenopus egg cytosol *Mol. Biol. Cell* **24** 1559–73
[23] Smith M B, Li H, Shen T, Huang X, Yusuf E and Vavylonis D 2010 Segmentation and tracking of cytoskeletal filaments using open active contours *Cytoskeleton* **67** 693–705
[24] Kumar N 1981 Taxol-induced polymerization of purified tubulin. Mechanism of action *J. Biol. Chem.* **256** 10435–41
[25] Bolhuis P G, Stroobants A, Frenkel D and Lekkerkerker H N W 1997 *J. Chem. Phys.* **107** 1551–64
[26] Frenkel D, Lekkerkerker H N W and Stroobants A 1988 *Nature* **332** 822–3

[27] Vroege G J and Lekkerkerker H N W 1992 *Rep. Prog. Phys.* **55** 1241
[28] Nedelec F and Foethke D 2007 Collective Langevin dynamics of flexible cytoskeletal fibers *New J. Phys.* **9** 427
[29] Culver Hanlon T L, Lex S A, Stephens A D, Quintyne N J and King S J 2006 A microtubule-binding domain in dynactin increases dynein processivity by skating along microtubules *Nat Cell Biol.* **8** 264–70
[30] Wang Q, Crevenna A H, Kunze I and Mizuno N 2014 Structural basis for the extended CAP-Gly domains of p150glued binding to microtubules and the implication for tubulin dynamics *Proc. Natl Acad. Sci.* **111** 11347–52
[31] Kunwar A *et al* 2011 *Proc. Natl Acad. Sci.* **108** 18960–5
[32] Schaffner S C and Jos J V 2006 *Proc. Natl Acad. Sci.* **103** 11166–71
[33] McKenney R J, Huynh W, Tanenbaum M E, Bhabha G and Vale R D 2014 *Science* **345** 337–41
[34] Valentine M T, Perlman Z E, Mitchison T J and Weitz D A 2005 *Biophys. J.* **88** 680–9
[35] Götz T and Unterreiter A 2000 *J. Integral Equations Appl.* **12** 225–70
[36] Tao Y G, Otter W K d, Padding J T, Dhont J K G and Briels W J 2005 *J. Chem. Phys.* **122** 244903
[37] Snook B, Davidson L M, Butler J E, Pouliquen O and Guazzelli É 2014 *J. Fluid Mech.* **758** 486–507